Time-Efficient Multi-Physics Optimization Approaches for the Design of Synchronous Reluctance Motors

Christophe De Gréef[1], Virginie Kluyskens[1], François Henrotte[1,2], Christophe Versèle[3], Christophe Geuzaine[2], Bruno Dehez[1]
[1]*Institute of Mechanics, Materials and Civil Engineering (IMMC)*
Université catholique de Louvain (UCLouvain), Louvain-la-Neuve, Belgium
[2]*Department of Electrical Engineering and Computer Science, Montefiore Institute*
Université de Liège (ULiège), Liège, Belgium
[3]*Alstom Belgium*, Charleroi, Belgium
E-mail: {christophe.degreef, virginie.kluyskens, francois.henrotte, bruno.dehez}@uclouvain.be,
{francois.henrotte, cgeuzaine}@uliege.be, christophe.andre.versele@alstomgroup.com

***Abstract*—The design of synchronous reluctance machines involves a multiphysics optimization with a consequent number of design parameters. To lower the optimization time, it is common to split the problem into subproblems, i.e., to optimize successively the flux barriers for the electromagnetic performance, and then the ribs for the structural integrity of the rotor. This however leads in general to a suboptimal design, because the cross-coupling between design parameter subsets (e.g., magnetic and mechanical) is this way ignored. In this study, different splitting optimization strategies have been implemented and evaluated by comparing not only the electromagnetic performance reached by the optimized designs, but also the computation time. Results show that the optimization time can indeed be significantly lowered by performing a magnetic optimization followed by a mechanical optimization, with little impact on the mean torque output. Pre-dimensioning analytically the radial ribs within the magnetic optimization further reduces the optimization time and improves the performance of the design. Finally, performing an additional iteration on the approach leads to a mean torque and torque ripple very close to the ones obtained by carrying the global optimization, with however half the optimization time.**

I. Introduction

The rotor of synchronous reluctance machines (SynRM) contains no other elements than ferromagnetic material. This simple structure reduces the manufacturing costs and improves their reliability. The absence of permanent magnets allows higher operating temperature and breaks free of the long-term availability and volatile costs of rare-earth materials. Moreover, the synchronous operation limits the rotor losses, hence leading to an intrinsic high efficiency.

The axially laminated anisotropic (ALA) rotor topology, proposed by Kostko [1] in 1923, is optimal for torque generation, but hardly practicable for its construction. The alternative transversally laminated anisotropic (TLA) rotor topology brings the construction of such a motor in-line with the industry standards, where identical laminations are punched and axially stacked. The structural integrity of the laminations is ensured by small ribs that link all the flux guides together. These ribs must be wide enough to withstand the magneto-mechanical loading the rotor is subjected to, but narrow enough to limit their negative impact on the magnetic performance of the machine. Indeed, these ribs act as a q-axis magnetic short circuit that lowers the d-q axis anisotropy of the rotor, hence limiting the torque output and the power factor of the machine.

As a consequence, the design of SynRM must be addressed considering both the magnetic and mechanical aspects. Computer-aided optimization is a very powerful tool to that end, unfortunately the computational cost climbs quickly as the design space grows. To reduce the optimization time, some authors propose to simply split the design space into smaller parts that will be optimized successively. For SynRM, this is often done by optimizing the flux barriers separately from the ribs, which are optimized at the end of the design approach to ensure the structural integrity of the rotor. For instance, in [2], a permanent magnet assisted SynRM has been designed over a torque-speed range using computationally inexpensive models. In [3], the structural reinforcement has been performed by both a parametric and a topology optimization. It is worth mentioning that the ribs optimization is often significantly faster than the flux barriers optimization, due to a very different evaluation time between the mechanical model and the magnetic model.

However, carrying successive optimizations naturally degrades the quality of the solution because it ignores the cross-coupling of the optimal parameters. The flux barriers characteristics do impact the mass distribution of the rotor and, by consequence, the mechanical load the ribs have to sustain. Comparably, adding ribs to the design does change the magnetic field distribution inside the rotor which affects the magnetic performance of the machine. Hence, the benefits of carrying successive optimizations on the total optimization time should be weighed against the impact on the quality of the solution. This is rarely discussed in the literature because

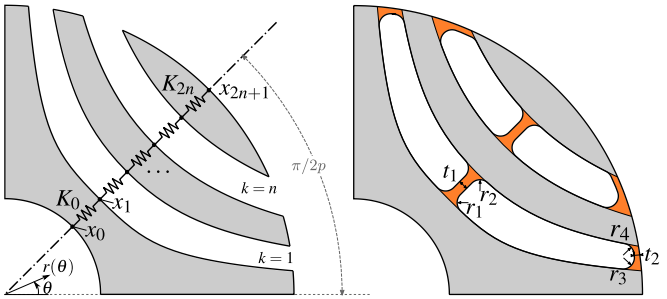

(a) (b)

Fig. 1. (a) Parametrization used to describe n flux barriers. (b) Parametrization used to describe the radial and tangential ribs. For a reason of clarity, only two flux barriers are represented.

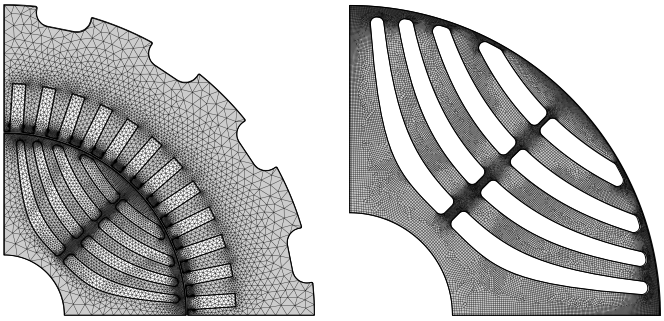

(a) (b)

Fig. 2. Example of meshes used to perform FE simulations. (a) Magnetic mesh (rotor + stator), that has around 28000 triangular elements. (b) Mechanical mesh (rotor only), that has around 35000 rectangular elements.

of its impracticability. Indeed, it involves the application of several design approaches that can have high computational costs.

In this study, several design approaches are applied to find the optimal parameters that will maximize the mean torque of the motor under the constraints of keeping the local mechanical stresses and the torque ripple limited. The total optimization time and the performance reached by each design are then compared.

In this paper, section II describes the parametrization of the geometry, section III the magnetic and mechanical finite element (FE) models used to assess its performance. The design approaches to obtain the optimal design are described in section IV, the optimization procedure in section V, and the results are finally given in section VI.

II. Geometry and Parametrization

The parametrization of the geometry is an essential step to perform the optimization. A wide design space is more potent to bring a better solution than a smaller design space, however it also introduces a greater computational cost and potential optimization convergence issues.

We focused the optimization on the rotor of a 4 poles motor, with 4 flux barriers per pole and a fixed stator. The parameters to optimize are divided into two categories: those describing the flux barriers, $\boldsymbol{x}_{\text{mag}}$, and those describing the ribs, $\boldsymbol{x}_{\text{mech}}$.

The flux barriers are parametrized using Joukowski airfoil potential function, written in cylindrical coordinates (r, θ) [4]:

$$r(\theta) = R_{in} \cdot \sqrt[p]{\frac{C + \sqrt{C^2 + 4\sin^2(p\theta)}}{2\sin(p\theta)}}, \tag{1}$$

with R_{in} the inner radius of the rotor, p the number of pole pairs, and C a constant depending on the x position of the curve along the symmetry line of the rotor, at $\theta = \pi/2p$:

$$C(x) = \frac{\left(\frac{x}{R_{in}}\right)^{2p} - 1}{\left(\frac{x}{R_{in}}\right)^{p}}. \tag{2}$$

As shown in Fig. 1(a), two Joukowski lines, located at different x, are needed to entirely describe the inner and outer boundaries of a flux barrier. Despite the limited number of parameters, studies have shown the excellent magnetic performance of such shape [5]–[7].

To prevent overlaps between flux barriers, their positions and thicknesses are determined indirectly with a set of virtual springs that repel constructive points that cannot meet, Fig. 1(a) [5]. The stiffnesses K_i of these springs are the new design parameters, which yields a parameter space with no other internal constraint than the positiveness of the stiffnesses. The relationship between the position of the i^{th} Joukowski line x_i and the stiffness K_i is:

$$x_i = x_{i-1} + \frac{K_i}{\sum_{k=0}^{2n} K_k}(x_{2n+1} - x_0). \tag{3}$$

On the other hand, the structural integrity of the rotor is ensured by tangential and radial ribs, placed as depicted in Fig. 1(b). Each rib is parametrized with a thickness t and circular fillets of radius r to prevent stress concentration, as shown in Fig. 1(b). Accounting for the ribs adds six parameters per flux barrier to the design space, i.e., three for the tangential ribs and three for the radial ribs.

III. Magnetic and Mechanical Evaluations

The electromagnetic performance of the machine is evaluated using a 2D quasi-static FE model. The nonlinear $B-H$ characteristic of the magnetic material is accounted for by using an iterative Newton-Raphson resolution scheme. The torque is obtained by the integration of the Maxwell stress tensor in the airgap. Simulations are carried out at 150 different rotor positions to properly capture the torque ripple. The phase of the sinusoidal currents are prescribed in coherence with the position increments to simulate the synchronous operation of the motor.

The model profits from the periodicity of the problem to lower the number of degrees of freedom (DoF). The resolution time is further reduced by using the moving band method. With this method, the rotor and stator geometry are meshed once, and the position increment simply consists in rotating the rotor mesh. Triangular mesh elements are then inserted

TABLE I
NOMINAL VALUES OF THE MOTOR

Param.	Value	Description
N_n	1500 rpm	Nominal speed
$N_{\max}$	4800 rpm	Maximum speed
j_n	$8.5\,\mathrm{A/mm^2}$	Nominal current density
p	2	Number of pole pairs
n	4	Number of flux barriers (per pole)

TABLE II
DESIGN SPACE BOUNDARIES $(i = 0, 1, ..., 2n)$, $(k = 1, 2, ..., n)$

Param.	Description	Lower bound	Upper bound	Unit
θ_e	Current angle	45	75	°
K_i	Virtual spring stiffness	1	10	–
$r_{1,k}$	Fillet radius 1	1	10	mm
$r_{2,k}$	Fillet radius 2	1	10	mm
$t_{r,k}$	Radial rib thickness	0	5	mm
$r_{3,k}$	Fillet radius 3	1	10	mm
$r_{4,k}$	Fillet radius 4	1	10	mm
$t_{t,k}$	Tangential rib thickness	0.3	8	mm

in the middle of the airgap to stitch the stator mesh with the rotor mesh. Because the meaning of each DoF is kept the same, the result of the previous position can directly be used as starting point of the new nonlinear resolution. That drastically lowers the iterations needed in the Newton-Raphson resolution scheme, which benefits the global resolution time.

The mechanical stresses are obtained by an other 2D FE model. The linear elasticity equations are solved on the rotor geometry, which is subjected to a centrifugal load.

Both these models use the mesh generator Gmsh [8] and the solver GetDP [9]. A fine discretization is used to keep the results as accurate as possible. An example of the meshes used during the optimization is shown in Fig. 2.

IV. DESIGN APPROACHES

Each design approach aims at finding the design parameters that maximize the mean torque $\overline{T}$ while keeping the relative torque ripple $\widetilde{T}$ below 10%, and the local Von-Mises stress σ_{VM} below $270\,\mathrm{MPa}$ at the maximum speed. The nominal values of the motor are given in Table I. With this current density, the current angle θ_e that maximizes the torque per ampere is no longer $45°$ because of the magnetic saturation the motor is subjected to. As a consequence, this parameter will also be optimized.

The full design space of the problem is presented in Table II. The upper part of this table is linked to the magnetism-related parameters, i.e., current angle, position and thicknesses of the flux barriers, and will be referred as $\boldsymbol{x}_{\mathrm{mag}}$. The lower part is linked to the mechanical-related parameters, i.e., thicknesses and fillets radii of the ribs, and will be referred as $\boldsymbol{x}_{\mathrm{mech}}$.

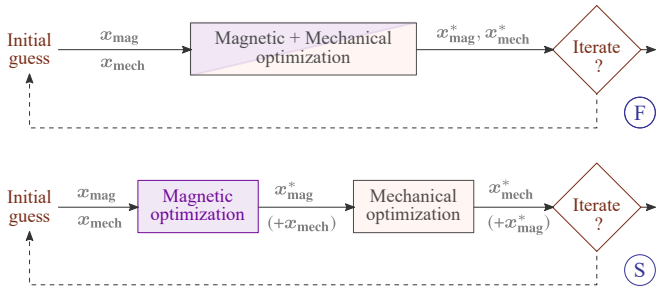

Fig. 3. Principle scheme of the two different design approaches. A single full optimization can be carried out (F), or it can be split in two successive optimizations (S). The superscript * is used to define parameters that have been optimized.

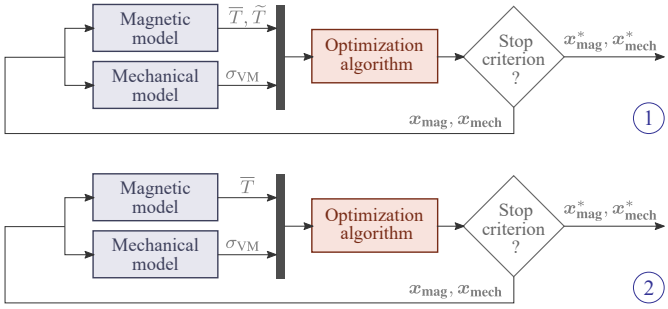

Fig. 4. Magneto-mechanical optimization variants (F approach).

Formally, the design problem is a multiphysics single objective two constraints problem, that can be written:

$$\begin{aligned} \max_{\boldsymbol{x}_{\mathrm{mag}}, \boldsymbol{x}_{\mathrm{mech}}} \quad & \overline{T}(\boldsymbol{x}_{\mathrm{mag}}, \boldsymbol{x}_{\mathrm{mech}}) \\ \text{s.t.} \quad & \max(\sigma_{\mathrm{VM}}) < 270\ \mathrm{MPa} \\ & \widetilde{T}(\boldsymbol{x}_{\mathrm{mag}}, \boldsymbol{x}_{\mathrm{mech}}) < 10\%. \end{aligned} \tag{4}$$

Two main approaches are investigated to tackle the optimization problem (4). As depicted in Fig. 3, the first approach (F) consists in carrying a single optimization on the full design space. The second approach (S) involves two successive optimizations, the first one dealing with $\boldsymbol{x}_{\mathrm{mag}}$ to maximize the mean torque under the torque ripple constraint, and the second one dealing with $\boldsymbol{x}_{\mathrm{mech}}$ to ensure the structural integrity of the rotor. The initial guess is chosen as a rotor having flux barriers the same thicknesses as the flux guides, and no ribs:

$$\begin{aligned} \boldsymbol{x}_{\mathrm{mag}} &= \begin{cases} \theta_e = 45 \\ K_i = 1 \quad (i = 0, 1, ..., 2n) \end{cases} \\ \boldsymbol{x}_{\mathrm{mech}} &= \boldsymbol{0}. \end{aligned} \tag{5}$$

The choice of the initial guess in the first approach (F) is not important as it provides parameters that are already included in the design space, so that there is also no need to iterate. However, iterating might help the optimization algorithm to escape local minima.

Contrarily, the choice of the initial guess is primordial in the second approach (S). Ideally, $\boldsymbol{x}_{\mathrm{mech}}$ should come as close as possible to the optimal value of the mechanical

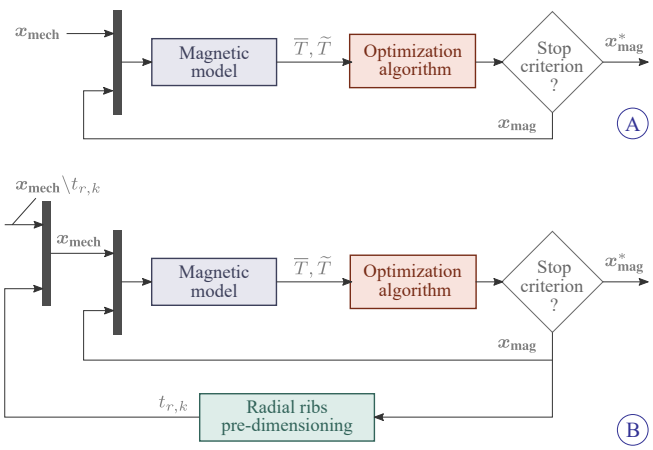

Fig. 5. Approaches investigated to perform the magnetic optimization.

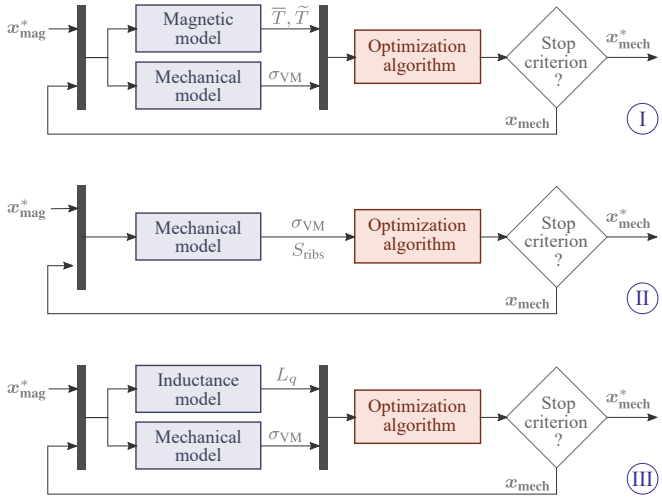

Fig. 6. Approaches investigated to perform the mechanic optimization.

parameters $\boldsymbol{x}^*_{\text{mech}}$, so that the electromagnetic performance of the design will not be deteriorated too much after performing the mechanical optimization. Iterating on the approach is expected to bring the initial guess $\boldsymbol{x}_{\text{mech}}$ closer to the optimal values $\boldsymbol{x}^*_{\text{mech}}$. In this study, two iterations are performed.

Beyond these two approaches, several variants of each optimization are considered in this study. They differ by their objectives and constraints.

The block schemes of the magneto-mechanical optimization variants are presented in Fig. 4. The variant 1 consists exactly in the optimization problem (4). The design that will be obtained using the approach F1 is expected to have the best performance, at the cost of a longer optimization time. The variant 2 consists in dropping the torque ripple constraint from the optimization problem:

$$\begin{aligned} \max_{\boldsymbol{x}_{\text{mag}}, \boldsymbol{x}_{\text{mech}}} \quad & \overline{T}(\boldsymbol{x}_{\text{mag}}, \boldsymbol{x}_{\text{mech}}) \\ \text{s.t.} \quad & \max(\sigma_{\text{VM}}) < 270 \text{ MPa}. \end{aligned} \tag{6}$$

The design obtained with this variant will most likely violate the torque ripple constraint, but it gives an estimation on how much mean torque is sacrificed to lower the torque ripple down to 10%.

Two magnetic optimization variants of the split approach (S) are represented in Fig. 5. The optimization problem is the same for both of them:

$$\begin{aligned} \max_{\boldsymbol{x}_{\text{mag}}} \quad & \overline{T}(\boldsymbol{x}_{\text{mag}})\Big|_{\boldsymbol{x}_{\text{mech}}} \\ \text{s.t.} \quad & \widetilde{T}(\boldsymbol{x}_{\text{mag}})\Big|_{\boldsymbol{x}_{\text{mech}}} < 10\%. \end{aligned} \tag{7}$$

However, the radial ribs thicknesses $t_{r,k}$ vary within the optimization of variant B. The radial ribs are pre-dimensioned analytically, as suggested in [10], to withstand the centrifugal loading the rotor is subjected to, which depends on the mass distribution of the rotor:

$$t_{r,k}(\boldsymbol{x}_{\text{mag}}) = \frac{M_k \omega_m^2 R_{G,k}}{\sigma_y} \cdot \text{SF}, \tag{8}$$

with M_k the mass the k^{th} rib has to withstand, $R_{G,k}$ the radius of its center of gravity, ω_m the rotational speed, σ_y the elasticity limit of the material, and SF a safety factor arbitrarily set to 1.5. The mass supported by the k^{th} rib is simply the combination of the mass of each flux guide m_j located after the rib:

$$M_k = \sum_{j=k}^{N} m_j \qquad R_{G,k} = \frac{\sum_{j=k}^{N} m_j R_{G,j}}{\sum_{j=k}^{N} m_j}, \tag{9}$$

with $R_{G,j}$ the center of gravity of the j^{th} flux guide.

The mechanical optimization that follows is expected to find an optimal value of $t^*_{r,k}$ that is close to $t_{r,k}(\boldsymbol{x}_{\text{mag}})$, so that performing the mechanical optimization should only have a moderate impact on the electro-magnetic performance of the machine.

The different variants of the mechanical optimization are represented in Fig. 6. The variant I consists in finding the parameters $\boldsymbol{x}_{\text{mech}}$ that maximize the mean torque, with the constraint of keeping the mechanical stresses below 270 MPa and the torque ripple under 10%:

$$\begin{aligned} \max_{\boldsymbol{x}_{\text{mech}}} \quad & \overline{T}(\boldsymbol{x}_{\text{mech}})\Big|_{\boldsymbol{x}^*_{\text{mag}}} \\ \text{s.t.} \quad & \max(\sigma_{\text{VM}}) < 270 \text{ MPa} \\ & \widetilde{T}(\boldsymbol{x}_{\text{mech}})\Big|_{\boldsymbol{x}^*_{\text{mag}}} < 10\%. \end{aligned} \tag{10}$$

This variant comes as close as possible to the initial optimization problem (4). However, it requires the torque evaluation of the machine through the magnetic model, which drastically increases the optimization time. One could imagine using a faster magnetic model to estimate $\overline{T}$ and $\widetilde{T}$, but the torque ripple $\widetilde{T}$ is so sensitive to the geometry that such a model would not provide satisfying results.

As an alternative, other objectives and constraints can be used to avoid the magnetic FE evaluations. The optimization variant II consists in minimizing the cumulative ribs surface

S_{ribs}, with the constraint of keeping the mechanical stresses below 270 MPa:

$$\begin{aligned} \min_{\boldsymbol{x}_{\text{mech}}} \quad & S_{\text{ribs}}(\boldsymbol{x}_{\text{mech}})|_{\boldsymbol{x}^*_{\text{mag}}} \\ \text{s.t.} \quad & \max(\sigma_{\text{VM}}) < 270 \text{ MPa}. \end{aligned} \tag{11}$$

This new optimization comes from the intuitive idea that minimizing the amount of material added inside the flux barriers should minimize the impact on the other quantities and, consequently, $\overline{T}$ and $\widetilde{T}$.

The optimization variant III consists in minimizing the q-axis inductance L_q, with the constraint of keeping the mechanical stresses below 270 MPa:

$$\begin{aligned} \min_{\boldsymbol{x}_{\text{mech}}} \quad & L_q(\boldsymbol{x}_{\text{mech}})|_{\boldsymbol{x}^*_{\text{mag}}} \\ \text{s.t.} \quad & \max(\sigma_{\text{VM}}) < 270 \text{ MPa}. \end{aligned} \tag{12}$$

Optimization problem (12) arises after dropping the torque ripple constraint from (10) and by using the torque equation of SynRMs [11]:

$$\overline{T} = \frac{3}{2}\, p\, (L_d - L_q)\, i_d i_q. \tag{13}$$

Under these conditions, the optimization problem (10) becomes:

$$\begin{aligned} \min_{\boldsymbol{x}_{\text{mech}}} \quad & -\frac{3}{2}\, p \left(L_d(\boldsymbol{x}_{\text{mech}})|_{\boldsymbol{x}^*_{\text{mag}}} - L_q(\boldsymbol{x}_{\text{mech}})|_{\boldsymbol{x}^*_{\text{mag}}} \right) i_d i_q \\ \text{s.t.} \quad & \max(\sigma_{\text{VM}}) < 270 \text{ MPa}. \end{aligned} \tag{14}$$

Removing the independent values with respect to $\boldsymbol{x}_{\text{mech}}$, and considering that the ribs have a negligible impact on the d-axis inductance L_d, the optimization problem (14) can be simplified to the optimization problem (12).

Although magnetism-related, the q-axis inductance L_q can be quickly estimated by a simple model presenting negligible computational cost. By assuming flux guides as perfect magnetic conductors and flux barriers as perfect magnetic insulators, the q-axis inductance is obtained by solving a magnetic circuit formed by the ribs. Radial and tangential ribs are parallel reluctance elements within the same flux barrier, which are put in series with the elements of the next flux barrier, as illustrated in Fig. 7. Each rib is approximated by a rectangular element of length l and cross-section $S = L \cdot t$, having a magnetic permeability μ. The reluctance of a rib is given by:

$$\mathcal{R} = \frac{l}{\mu \cdot S}. \tag{15}$$

The permeability is assumed to be identical in all the elements and independent of the rib dimensions. Under this assumption, the solution of the optimization problem (12) is independent of the magnetic permeability μ.

V. Optimization

A non-dominated sorting genetic algorithm-II (NSGA-II) [12] with a population size of 100 is used to solve the optimization problems. The mutation rate is set to 3%.

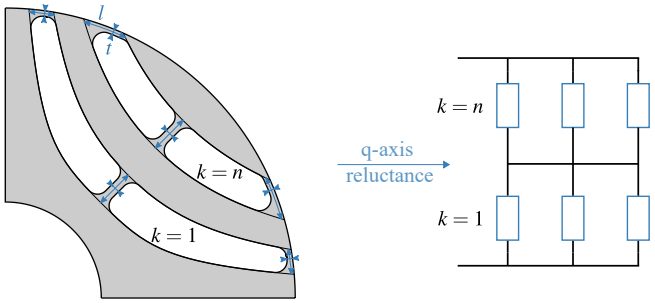

Fig. 7. Equivalent q-axis reluctance. The flux guides are considered infinitely permeable, and the ribs are approximated by rectangular elements.

These calculations are carried out using the Intel i9-7940X CPU (14 cores, 4.3 GHz). Concurrent evaluations of individuals of the same generations are performed to reach a near 100% CPU load. On average, it took 47.25 s for the magnetic model to evaluate the torque characteristics of the machine, and 3.15 s for the mechanical model to evaluate the local Von Mises stresses.

The optimization stops if the relative change in the objective function over the last 30 generations is less than 0.01%.

VI. Results

To avoid any confusion between the results, the magneto-mechanical optimization variants are designated using arabic numbers (Fig. 4), the magnetic optimization variants using capital letters (Fig. 5), and the mechanical optimization variants using roman numbers (Fig. 6). So that, for instance, the approach BII consists in a split design approach in which the magnetic optimization B is paired with the mechanical optimization II. An additional iteration on this approach will be written BII-BII. Naturally, only the approaches that end with either 1, 2, I, II, or III, lead to realistic designs that can sustain the mechanical load. Intermediate steps finishing by A or B are excluded from the presented results.

Moreover, the stochastic nature of the optimization algorithm must not be ignored. This randomness is expected to have a limited impact on approaches that consist in a single optimization of the full design space, i.e., approaches 1 & 2. Indeed, NSGA-II is a global search algorithm so that performing successive runs of the same optimization is supposed to bring solutions that are very close in terms of performance, although the underlying set of parameters $[\boldsymbol{x}^*_{\text{mag}}, \boldsymbol{x}^*_{\text{mech}}]$ might differ significantly due to the presence of local minima.

This impact could be more important for design approaches that consider successive optimizations, because of the cross-coupling that exists between the set of parameters that are optimized independently. Indeed, nothing indicates that a mechanical optimization on $\boldsymbol{x}_{\text{mech}}$ given a set of parameter $\boldsymbol{x}_{\text{mag,1}}$ will lead to the same performance than the same optimization given a set of parameters $\boldsymbol{x}_{\text{mag,2}}$, regardless of the optimization algorithm.

To account for the cross-coupling between $\boldsymbol{x}_{\text{mag}}$ and $\boldsymbol{x}_{\text{mech}}$ and the stochastic nature of the optimization algorithm, the

TABLE III

RESULTS OF THE SPLIT DESIGN APPROACHES, NORMALIZED P.U. ACCORDINGLY TO TABLE IV. THE QUANTITIES OF INTEREST ARE AVERAGED OVER THE DIFFERENT RUNS OF THE SAME APPROACHES. ALSO, THE LOWEST AND HIGHEST VALUES ARE REPORTED AS A DISPERSION INDICATOR.

Design approach	Mean torque	Torque ripple	Total optimization time	Design approach	Mean torque	Torque ripple	Total optimization time
AI	$0.91\ ^{+0.05}_{-0.05}$	$1.00\ ^{+0.00}_{-0.00}$	$0.97\ ^{+0.35}_{-0.24}$	BI	$0.92\ ^{+0.03}_{-0.04}$	$1.00\ ^{+0.00}_{-0.00}$	$0.41\ ^{+0.01}_{-0.01}$
AI-AI	$0.93\ ^{+0.03}_{-0.02}$	$0.99\ ^{+0.01}_{-0.01}$	$1.50\ ^{+0.45}_{-0.32}$	BI-BI	$0.94\ ^{+0.03}_{-0.04}$	$0.99\ ^{+0.01}_{-0.01}$	$1.07\ ^{+0.07}_{-0.13}$
AII	$0.96\ ^{+0.02}_{-0.04}$	$1.72\ ^{+0.45}_{-0.27}$	$0.48\ ^{+0.23}_{-0.25}$	BII	$0.97\ ^{+0.02}_{-0.03}$	$1.75\ ^{+0.13}_{-0.15}$	$0.17\ ^{+0.01}_{-0.01}$
AII-AII	$0.90\ ^{+0.01}_{-0.03}$	$1.46\ ^{+1.00}_{-1.11}$	$0.77\ ^{+0.28}_{-0.23}$	BII-BII	$1.00\ ^{+0.01}_{-0.01}$	$1.39\ ^{+0.39}_{-0.73}$	$0.55\ ^{+0.21}_{-0.12}$
AIII	$0.95\ ^{+0.03}_{-0.03}$	$2.30\ ^{+0.31}_{-0.16}$	$0.52\ ^{+0.20}_{-0.25}$	BIII	$0.97\ ^{+0.01}_{-0.02}$	$2.08\ ^{+0.32}_{-0.47}$	$0.18\ ^{+0.01}_{-0.02}$
AIII-AIII	$0.91\ ^{+0.01}_{-0.01}$	$1.19\ ^{+0.29}_{-0.33}$	$0.74\ ^{+0.18}_{-0.28}$	BIII-BIII	$0.97\ ^{+0.02}_{-0.01}$	$1.33\ ^{+0.39}_{-0.44}$	$0.43\ ^{+0.01}_{-0.02}$

TABLE IV

RESULTS FOR DESIGN APPROACHES 1 & 2.

Design approach	Mean torque		Torque ripple		Total optimization time	
	Nm	p.u.	%	p.u.	Hours	p.u.
1	1250.1	1	10.00	1	302	1
2	1258.4	1.01	36.60	3.66	151	0.5

approaches that consider successive optimizations are applied 3 times, i.e., approaches AI, AII, AIII, BI, BII, BIII, and their iterations. The average values of the quantities of interest are used for comparison purpose, while the dispersion gives information on how repeatable the design approach is.

The results of design approaches 1 & 2 are reported in Table IV. The design approach 1 serves as normalization of all the other results, as it directly implements the optimization problem (4). Dropping the torque ripple constraint, i.e., approach 2, does not seem beneficial. It only increases the mean torque by a negligible amount with a consequent increase of the torque ripple. The optimization time, however, has been halved.

The results of the split approaches are presented in Table III. Only the approaches I explicitly accounts for the torque ripple during the mechanical optimization, so that the obtained torque ripple is perfectly mastered. However, the mean torque is significantly reduced and the gain on the total optimization time is either not significant after the first iteration (approaches AI and BI), or even negative after the second iteration (approaches AI-AI and BI-BI). As a conclusion, these approaches are less interesting than approach 1 and should not be considered.

An other observation is that approaches B systematically lead to a lower total optimization time than approaches A. To better compare the mean torque and torque ripple of the remaining approaches, an other visualization of the data is presented in Fig. 8. In this visualization, the points belonging to the same approach are linked together to form triangles. The

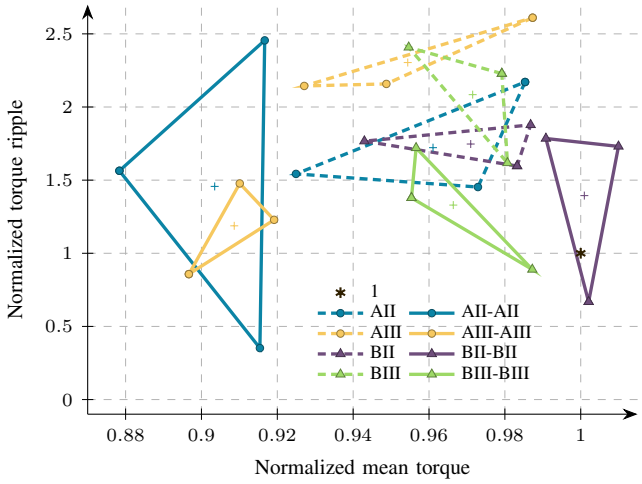

Fig. 8. Performance of the design obtained by the different approaches. The points belonging to independent runs of the same approach have been linked together for visualization purpose. The centers of gravity of the triangles, whose coordinates correspond to the averaged mean torque and torque ripple presented in Table III, are marked with a +.

averaged mean torque and averaged torque ripple correspond to the $x-y$ coordinates of the center of gravity of the triangle, whereas the dispersion is directly linked to the size of the triangle.

The first iteration of approaches AII, BII, AIII, BIII, corresponding to the dashed triangles, are quite similar in terms of reached performance. However, this observation is no longer true for the second iteration, corresponding to the solid triangles. With this second iteration, approaches B always lead to better performance than approaches A, which confirms that pre-dimensioning the ribs during the magnetic optimization is beneficial for the mechanical optimization that follows. Furthermore, approaches II dominate approaches III in terms of averaged values and/or spread of these values. This indicates that the simpler objective function II, which minimizes the cumulative rib surface, better captures the impact ribs have on the torque than the objective function III, which minimizes the

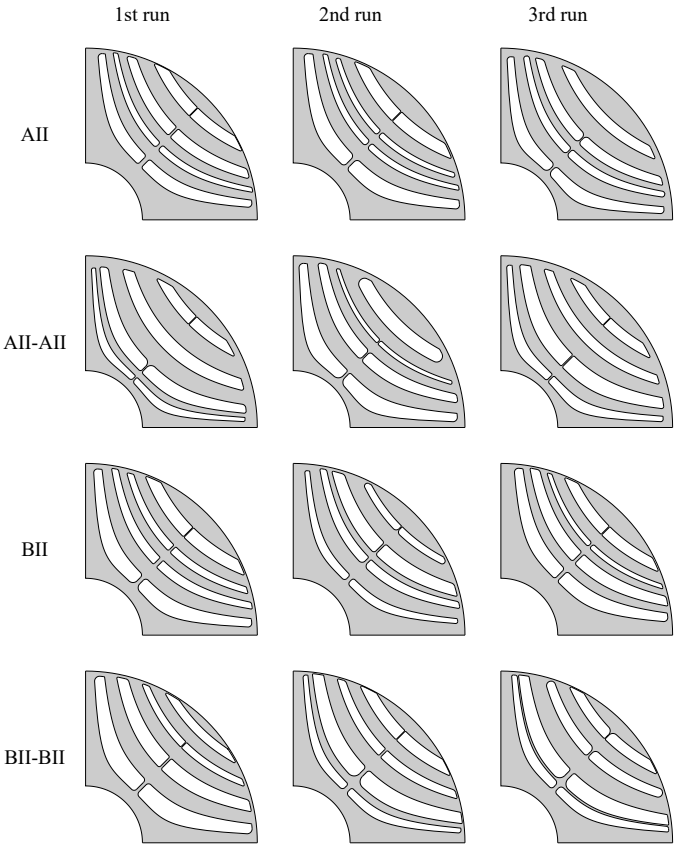

Fig. 9. Geometries obtained after performing three times the approaches AII, AII-AII, BII, BII-BII.

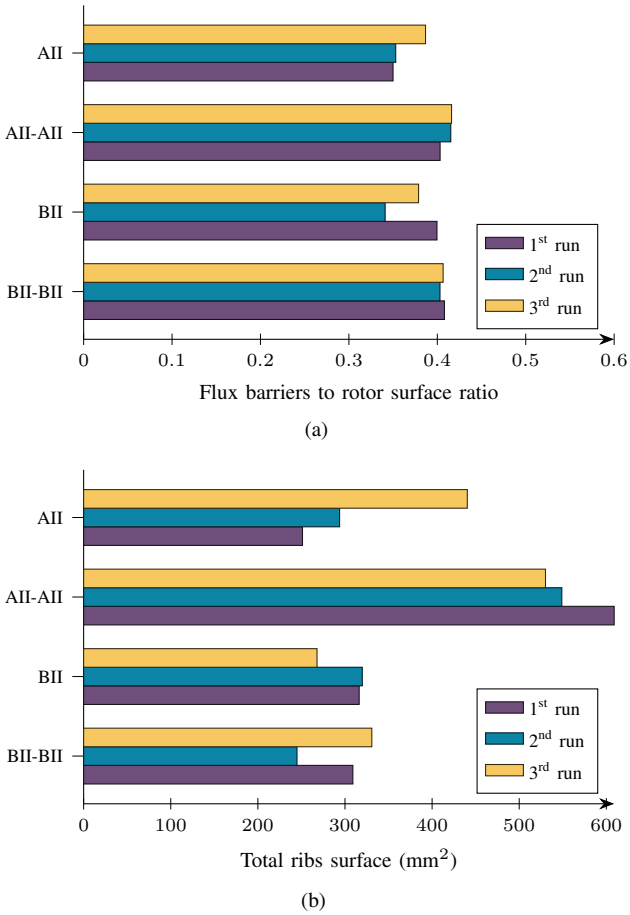

Fig. 10. (a) Flux barriers to rotor surface ratio and (b) total ribs surface of the geometries presented in Fig. 9.

q-axis inductance L_q. Although counter-intuitive, this result arises from a flawed evaluation of L_q by the simplified model presented in Fig. 7. With this model, the impact of the fillets is ignored, while approach II considers them through the ribs surface.

Moreover, design approach BII-BII seems a strong alternative to the reference approach 1. In average, the design obtained by this approach presents an equivalent mean torque for half the total optimization time. As for all the approaches II and III, the torque ripple is expected to violate the torque ripple constraint. Its value, however, is kept bounded to a relatively low level.

The optimal geometries obtained by approaches AII and BII, and with their second iteration, are presented in Fig. 9. It is interesting to observe how different geometries are between them. This is also true for geometries belonging to different runs of the same approach, although geometrical similarities are expected if they output the same torque.

It is possible to explain these results after rewriting the torque equation (13):

$$\overline{T} = \frac{3}{2}\, p \cdot \frac{L_d}{L_q}\left(L_q - \frac{L_q^2}{L_d}\right) \cdot i_d i_q \tag{16}$$

$$= \frac{3}{2}\, p \cdot \zeta \left(L_q - \frac{1}{\zeta} L_q\right) \cdot i_d i_q \tag{17}$$

$$= \frac{3}{2}\, p \cdot (\zeta - 1)\; L_q \cdot i_d i_q. \tag{18}$$

By attributing the saliency ratio ζ to the flux barriers to rotor surface ratio, and the q-axis inductance to the total ribs surface, we get a relation between the rotor geometry and the torque output of the machine.

Plotting these two quantities (Fig. 10) reveals similarities between geometries belonging to different runs of the same design approach. Moreover, the second iteration on approach BII tends to leave the total ribs surface unmodified while increasing the size of the flux barriers, whereas approach AII-AII tends to increase both the total ribs surface and the size of the flux barriers. This joins the observation performed on Fig. 8, where the second iteration marked a split on the mean torque output of approaches A and B. Also, the dispersion of these geometrical quantities are lessened after the second iteration. That indicates a convergence on the design approach upon iterating. Once again, this observation can be confirmed on Fig. 8 by examining the x-axis spread of the considered design approach before and after the iteration.

Finally, Fig. 11 shows the local Von Mises stress distribution and the instantaneous torque of designs obtained by approaches 1 and BII-BII. As expected, critical stresses are

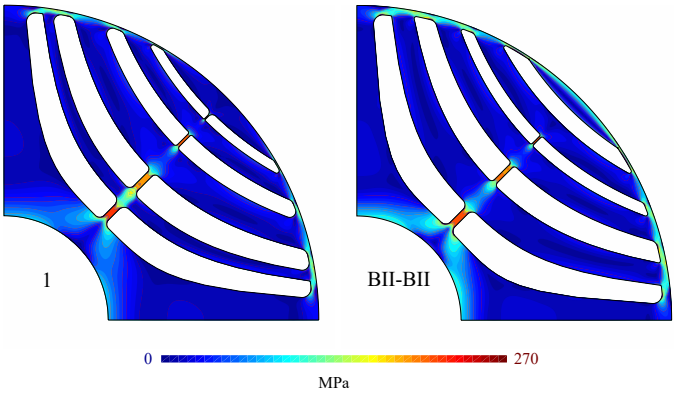

Fig. 11. Local Von Mises stress distribution.

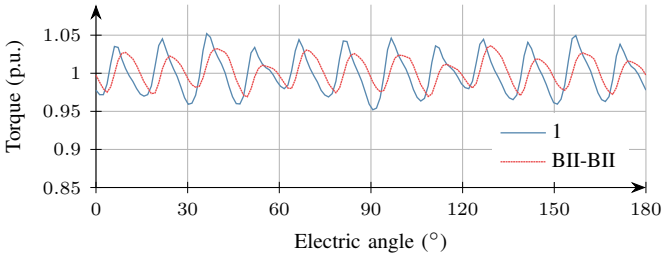

Fig. 12. Instantaneous torque during the synchronous operation of the motor.

localized in the fillets of the ribs and do not exceed 270 MPa. Similarly, the torque, Fig. 12, shows a ripple that does not exceed 10 % of the mean torque.

VII. Conclusion

Computer-aided design of SynRMs to ensure high mean torque, low torque ripple, and limited local stresses, is a time consuming process. This study shows that this computational cost can be reduced by relaxing the torque ripple constraint and by performing successive optimizations on subsets of the initial design space. A magnetic optimization is performed on the flux barriers to obtain the best magnetic performance, and is followed by a mechanical optimization on the ribs to ensure the structural integrity of the rotor. The objective function of the mechanical optimization can be as simple as minimizing the cumulative ribs surface (approaches II). To further reduce the total optimization time and to improve the performance of the obtained design, pre-dimensioning the ribs within the magnetic optimization should be considered (approaches B). Moreover, performing an additional iteration brings the electromagnetic performance of the design very close to the one obtained by considering a single optimization, for half the total optimization time.

VIII. Acknowledgment

This work was supported by the Walloon Region of Belgium under grant Traction2020.

References

[1] J. K. Kostko, "Polyphase reaction synchronous motors," *Journal of the American Institute of Electrical Engineers*, vol. 42, no. 11, pp. 1162–1168, 1923.

[2] C. López-Torres, A. Garcia, J. Riba, G. Lux, and L. Romeral, "Computationally efficient design and optimization approach of pma-synrm in frequent operating torque–speed range," *IEEE Transactions on Energy Conversion*, vol. 33, no. 4, pp. 1776–1786, 2018.

[3] A. Credo, G. Fabri, M. Villani, and M. Popescu, "High speed synchronous reluctance motors for electric vehicles: a focus on rotor mechanical design," in *2019 IEEE International Electric Machines Drives Conference (IEMDC)*, 2019, pp. 165–171.

[4] M. Palmieri, M. Perta, F. Cupertino, and G. Pellegrino, "Effect of the numbers of slots and barriers on the optimal design of synchronous reluctance machines," in *2014 International Conference on Optimization of Electrical and Electronic Equipment (OPTIM)*, May 2014, pp. 260–267.

[5] C. D. Gréef, V. Kluyskens, F. Henrotte, C. Geuzaine, and B. Dehez, "Impact of flux barriers shape in synchronous reluctance machine optimization," in *2019 19th International Symposium on Electromagnetic Fields in Mechatronics, Electrical and Electronic Engineering (ISEF)*, 2019, pp. 1–2.

[6] R. Rajabi Moghaddam, "Synchronous reluctance machine (synrm) in variable speed drives (vsd) applications," Ph.D. dissertation, KTH, Electrical Machines and Power Electronics (closed 20110930), 2011, qC 20110518.

[7] A. Dziechciarz and C. Martis, "New shape of rotor flux barriers in synchronous reluctance machines based on zhukovski curves," in *2015 9th International Symposium on Advanced Topics in Electrical Engineering (ATEE)*, 2015, pp. 221–224.

[8] C. Geuzaine and J.-F. Remacle, "Gmsh: A 3-d finite element mesh generator with built-in pre- and post-processing facilities," *International Journal for Numerical Methods in Engineering*, vol. 79, pp. 1309 – 1331, 09 2009.

[9] P. Dular, C. Geuzaine, F. Henrotte, and W. Legros, "A general environment for the treatment of discrete problems and its application to the finite element method," *IEEE Transactions on Magnetics*, vol. 34, no. 5, pp. 3395–3398, Sep. 1998.

[10] C. Babetto, G. Bacco, and N. Bianchi, "Synchronous reluctance machine optimization for high-speed applications," *IEEE Transactions on Energy Conversion*, vol. 33, no. 3, pp. 1266–1273, 2018.

[11] T. Matsuo and T. A. Lipo, "Rotor design optimization of synchronous reluctance machine," *IEEE Transactions on Energy Conversion*, vol. 9, no. 2, pp. 359–365, 1994.

[12] K. Deb, A. Pratap, S. Agarwal, and T. Meyarivan, "A fast and elitist multiobjective genetic algorithm: NSGA-II," *IEEE Transactions on Evolutionary Computation*, vol. 6, no. 2, pp. 182–197, April 2002.